1521-009X/51/3/403–412$35.00
Drug Metabolism and Disposition
dx.doi.org/10.1124/dmd.122.001049
Drug Metab Dispos 51:403–412, March 2023

Intravital Microscopy Reveals Unforeseen Biodistribution Within the Liver and Kidney Mechanistically Connected to the Clearance of a Bifunctional Antibody[S]

Amita Datta-Mannan, Bruce A. Molitoris, Yiqing Feng, Michelle M. Martinez, Ruben M. Sandoval, Robin M. Brown, Daniel Merkel, Johnny E. Croy, and Kenneth W. Dunn

Exploratory Medicine and Pharmacology (A.D-M.), Clinical Laboratory Services (R.M.B.), and Biotechnology Discovery Research (Y.F., D.M., J.E.C.), Lilly Research Laboratories, Indianapolis, Indiana and Department of Medicine, Division of Nephrology, Indiana University School of Medicine, Indianapolis, Indiana (K.W.D.)

Received August 3, 2022; accepted November 7, 2022

ABSTRACT

Bifunctional antibody (BfAb) therapeutics offer the potential for novel functionalities beyond those of the individual monospecific entities. However, combining these entities into a single molecule can have unpredictable effects, including changes in pharmacokinetics that limit the compound's therapeutic profile. A better understanding of how molecular modifications affect in vivo tissue interactions could help inform BfAb design. The present studies were predicated on the observation that a BfAb designed to have minimal off-target interactions cleared from the circulation twice as fast as the monoclonal antibody (mAb) from which it was derived. The present study leverages the spatial and temporal resolution of intravital microscopy (IVM) to identify cellular interactions that may explain the different pharmacokinetics of the two compounds. Disposition studies of mice demonstrated that radiolabeled compounds distributed similarly over the first 24 hours, except that BfAb accumulated approximately two- to -three times more than mAb in the liver. IVM studies of mice demonstrated that both distributed to endosomes of liver endothelia but with different kinetics. Whereas mAb accumulated rapidly within the first hour of administration, BfAb accumulated only modestly during the first hour but continued to accumulate over 24 hours, ultimately reaching levels similar to those of the mAb. Although neither compound was freely filtered by the mouse or rat kidney, BfAb, but not mAb, was found to accumulate over 24 hours in endosomes of proximal tubule cells. These studies demonstrate how IVM can be used as a tool in drug design, revealing unpredicted cellular interactions that are undetectable by conventional analyses.

SIGNIFICANCE STATEMENT

Bifunctional antibodies offer novel therapeutic functionalities beyond those of the individual monospecific entities. However, combining these entities into a single molecule can have unpredictable effects, including undesirable changes in pharmacokinetics. Studies of the dynamic distribution of a bifunctional antibody and its parent monoclonal antibody presented here demonstrate how intravital microscopy can expand our understanding of the in vivo disposition of therapeutics, detecting off-target interactions that could not be detected by conventional pharmacokinetics approaches or predicted by conventional physicochemical analyses.

Introduction

Multi- or bifunctional antibodies (BfAbs) are an emerging class of biotherapeutics. Unlike monoclonal antibodies (mAbs), which typically target one epitope, BfAbs recognize at least two different epitopes or antigens within a single moiety, often through an obligate physical linkage of the binding components. These interactions can expand and prolong BfAb efficacy. Advances in protein engineering have enabled significant innovations in BfAb formats by leveraging the modular structure of their counterpart mAbs (Labrijn et al., 2019; Ma et al., 2021). The IgG-like BfAbs, including IgG-extracellular domain (ECD) formats, consist of target-binding subunits attached to a mAb (Sedykh et al., 2018).

Although BfAbs have immense therapeutic promise and structural tractability, the translation of these modalities as medicines has been relatively slow compared with mAbs, with approvals for amivantamab, emicizumab, and blinatumomab occurring recently. Like most therapeutics, the causalities of BfAb slow clinical success can be generally related to several factors, including an incomplete understanding of the biologic mechanism of action and exposure–response profiles, insufficient safety margins, strategic industry decisions, and immunogenicity. The higher structural diversity of the BfAbs also results in greater uncertainty in their pharmacokinetic (PK) and disposition profiles that could limit their potential advantages (Khawli et al., 1996, 2010; Boswell et al., 2012, 2013; Tibbitts et al., 2016; Datta-Mannan et al., 2016, 2019; Datta-Mannan et al., 2019; Rock and Foti 2019; Datta-Mannan et al., 2021). As such, consideration of dynamic evaluations of BfAb tissue and cellular biodistribution profiles and how these are connected to their clearance are warranted.

This work was funded by Eli Lilly & Company.

A.D-M., Y.F., R.M.B., D.M., and J.E.C. are employees and recipients of Eli Lilly & Company stock. The other authors have no actual or perceived conflict of interest with the contents of this article.

dx.doi.org/10.1124/dmd.122.001049.

[S] This article has supplemental material available at dmd.aspetjournals.org.

ABBREVIATIONS: BfAb, bifunctional antibody; ECD, extracellular domain; DL594, DyLight594; DTPA, diethylene triamine pentaacetic acid; HC, heavy chain; IVM, intravital microscopy; mAb, monoclonal antibody; PK, pharmacokinetic; VEGF, vascular endothelial growth factor.

Integration of quantitative whole-body biodistribution and tissue-level imaging into the development can provide informative readouts regarding the disposition (Khawli et al., 1996; Khawli et al., 2010; Boswell et al., 2012; Boswell et al., 2013; Datta-Mannan 2019). Toward this, a handful of imaging approaches including, computed tomography, magnetic resonance imaging, whole-body imaging bioluminescence/radiolabeling, and positron emission tomography have been leveraged (Boswell et al., 2013, 2019; Datta-Mannan et al., 2016, 2019, 2021; Williams et al., 2016). While these imaging techniques offer a high degree of sensitivity and enable some quantitative measurements of the PK–pharmacodynamic relationship, they lack spatial and temporal resolution; thus, multiple approaches are required to characterize the connectivity of disposition to pharmacology (Wang et al., 2018). Often, for cellular distribution resolution, this requires orthogonal histologic evaluations. These evaluations involve sacrificing animals and can be laborious in terms of identifying reagents, are unidimensional, and have the potential for artifactual findings (Wang et al., 2018).

Advances in the field of nonlinear microscopy have made intravital multiphoton microscopy (IVM) an important tool, combining high-sensitivity and high-spatiotemporal resolution to provide a unique window into the dynamics of cell biology in living animals (Dunn and Day 2017; Nobis et al., 2018). IVM offers a novel approach to examining real-time molecular behavior within intact organs, providing insights into cellular and subcellular transport that complement radiolabel biodistribution approaches. In the present study, we combined quantitative whole-body radiolabel studies with IVM to gain insight into the real-time dynamic disposition and uptake/elimination of a BfAb and its counterpart parental mAb within major organs of elimination as a means to dissect the mechanisms influencing the in vivo tissue and cellular and subcellular distribution of the molecules.

An IgG–ECD BfAb architecture made with ECD and mAb units targeting two distinct soluble ligands, which have negligible peripheral concentrations in normal animals, was used for the present work so disposition and cellular trafficking dynamics could be evaluated without target-mediated drug disposition. This BfAb, deemed G_41-C-HC, has the D2 domain of vascular endothelial growth factor (VEGF) receptor 1 as the ECD fusion partner, connected via a flexible glycine–serine linker to the C-terminal end of the heavy chain (HC) of an IgG_4-based parent (G_41-) mAb (Supplemental Fig. 1) (Datta-Mannan et al., 2019). In earlier studies, G_41-C-HC showed inferior PK properties in mice relative to the parental G_41- mAb (Datta-Mannan et al., 2019). Herein, studies with a radiometal chelating tissue residualizing probe, which can accumulate within tissues if constructs are catabolized intracellularly, showed that PK differences were connected to early enhanced association and accumulation of the G_41-C-HC construct within the liver and kidney. While the tissue concentration disparities between the molecules were observed at times <24 hours post-administration, the blood exposures at ≤24 hours were perplexingly similar between the molecules. Thus, the mechanistic basis of the later differences in clearance was further addressed using fluorescence-based dynamic IVM in kidneys and liver.

The IVM studies revealed three key insights: (i) fluorescent conjugates of G_41-C-HC BfAb clear faster from the circulation than corresponding fluorescent conjugates of G_41 mAb during the first 24 hours post-dose; (ii) both compounds are internalized into sinusoidal endothelia in the liver but with strikingly different kinetics; (iii) G_41-C-HC BfAb (but not G_41 mAb) accumulates dramatically in endosomes of the proximal tubule epithelia. While the basis for these differences is unclear, they appear to reflect differences in how the two compounds interact with the endocytic systems of the liver and kidney. Taken together, these results highlight the importance of exploring the dynamics of tissue, cellular, and subcellular disposition for understanding the mechanistic basis of biologics clearance and elimination to improve drug ability.

Materials and Methods

Expression and Purification of Monoclonal and Bispecific-Antibody Molecules. The mAb and BfAb described within this report were expressed in either transient HEK-293 or stably transfected Chinese hamster ovary cells that were generated at Eli Lilly and Company (Indianapolis, IN, USA) as described elsewhere (Datta-Mannan et al., 2016, 2019).

Dylight594 Fluorescent Probe Labeling of Monoclonal and Bispecific-Antibody Molecule. G_41 mAb and G_41-C-HC BfAb were both labeled with DyLight594 (DL594) NHS Ester (Thermo Fisher, Waltham, MA, USA). The DL594 dye was dissolved in DMSO to a concentration of 9.3 mM. A 3× molar excess of dye was added to either G_41 mAb or G_41-C-HC BfAb, and the reaction mixtures were incubated at room temperature for 1 hour to achieve an average dye to G_41 mAb or G_41-C-HC BfAb ratio of 1.6 and dye to G_41-C-HC BfAb ratio of 1.0. Removal of excess dye was accomplished using preparative size exclusion chromatography (GE 16/60 HiLoad Superdex 200pg) while buffer exchanging into Gibco 1×PBS pH 7.2 buffer.

In Vitro Characterization of the Fluorescently Labeled Monoclonal and Bispecific Antibody. Electrostatic interactions of G_41 mAb or G_41-C-HC BfAb were measured using a heparin chromatographic method as described in Datta-Mannan et al. (2016). The extent of heparin sulfate binding was assessed by the observed column retention time and the corresponding sodium chloride concentration to elute the bound protein from the column.

The global hydrophobicity of the molecules evaluated in this study was assessed using hydrophobic interaction chromatography methods as described previously (Datta-Mannan, et al., 2016). The hydrophobicity of the molecules was inferred based on the observed column retention (measured in minutes) and the corresponding minimal ammonium sulfate concentration required for column retention.

The binding of fluorescently labeled G_41- mAb or G_41-C-HC BfAb to rat FcRn was measured at pH 6 in a microscale thermophoresis assay as previously described (Wagner et al., 2016).

Exposure Evaluation of DL594 Labeled and Unlabeled Monoclonal and Bispecific Antibody Molecules in Rats. A Sprague–Dawley rat exposure study was conducted following standard operating procedures and the protocol as approved by the Covance (now Labcorp, Madison, WI, USA) institutional review board and in compliance with the requirements of Eli Lilly and Company. The exposure study was performed with male rats (approximately 300–350 g) with the DL594-labeled and DL594-unlabeled versions of the G_41 mAb and G_41-C-HC BfAb molecules. Three rats were assigned to each study group, and all animals received a single intravenous bolus dose of either DL594-labeled or DL594-unlabeled G_41 mAb and DL594-labeled or DL594-unlabeled G_41-C-HC BfAb dissolved in PBS (pH, approximately 7.4) at 1.0 mg/kg. Each animal had blood samples collected via a jugular vein at 0.083, 1, 6, 12, and 24 hours after administration of the dose. Additionally, blood samples for the DL594-labeled G_41 mAb and DL594-labeled G_41-C-HC BfAb were also collected at 48, 72, and 96 hours post-dose. All the blood samples were collected into tubes containing K_3EDTA maintained in chilled cyroracks and centrifuged to obtain plasma. Concentrations of the labeled and unlabeled G_41 mAb and G_41-C-HC BfAb molecules in rat plasma were determined using anti-human IgG ELISAs as previously described (Datta-Mannan et al., 2019). Plasma concentration-time data following intravenous administration for the labeled constructs were described using a noncompartmental method according to the statistical moment theory using Phoenix WinNonlin software package (Pharsight, A Certara Company, St. Louis, MO, USA). The parameters calculated included the maximum serum concentration (C_{max}) and area under the curve ($AUC_{0-\infty}$), clearance (CL), and elimination half-life ($t_{1/2}$).

Murine Biodistribution Study With Radiolabeled G_41 mAb and G_41-C-HC BfAb Using a Tissue Residualizing Agent. A murine tissue distribution study was conducted following standard operating procedures, and the protocol as approved by Eli Lilly and Company and in compliance with the requirements contained in the MPI Research (now Charles River, Mattawan, MI, USA) Radioactive Materials License Number 21-11315-02, and all applicable regulations issued by the Nuclear Regulatory Commission as described previously (Datta-Mannan et al., 2019). Briefly, the non-radiolabeled G_41 mAb and G_41-C-HC BfAb were conjugated to diethylene triamine pentaacetic acid (DTPA) and radiolabeled with ^{111}In at MPI Research, Inc. (now Charles River, Mattawan, MI, USA) to target a low specific activity using previously published

radiochemistry approaches (Boswell et al., 2010). The dosing formulations were administered once via intravenous injection into the tail vein to a target dose level of 2 mg/kg (15 μCi/animal). Blood samples were collected at 1, 6, 12, and 24 hours post-dose (cohorts of two animals per group), processed to plasma, and analyzed as reported in earlier studies (Datta-Mannan et al., 2019). Tissues including adrenal gland, bladder (urinary), bone (femur), bone marrow (femur), brain, muscle (gastrocnemius, both quadriceps, and scapular region), heart, kidney, large intestine/cecum with contents, liver, lung, lymph nodes (mesenteric), pancreas, skin (ventral and upper and lower dorsal), small intestine with contents, spleen, stomach with contents, testes, thymus, thyroid, and fat pad were also collected and analyzed from two animals per time point (1, 6, 12, and 24 hours post-dose) as reported previously (Datta-Mannan et al., 2019). Individual gamma radioactivity counts were used for image reconstruction and analysis.

Intravital Microscopy Studies in Mice and Rats. Intravital microscopy studies of mice used either Lys-EGFP (Faust et al., 2000) or C57BL/6N (Jackson Laboratories, Bar Harbor, ME, USA) strains (23–30 g, 7–10 weeks of age). The Lys-EGFP mice express EGFP under the control of the Lys promoter, resulting in the expression of EGFP by myelomonocytic cells. Intravital microscopy studies of rats used Munich–Wistar–Fromter rats (9–12 weeks of age) from a colony maintained at Indiana University that was originally derived from animals generously provided by Dr. Roland Blantz (UC San Diego). All animals were maintained at the Indiana University LARC facility and were provided with food and water ad libitum. All animal experiments were approved and conducted according to the Institutional Animal Care and Use Committee guidelines of Indiana University and adhered to the guide for the care and use of animals (National Research Council Committee for the Update of the Guide for the Care and Use of Laboratory Animals et al., 2011).

Fluorescent probes used for intravital microscopy studies included Hoechst 33342 trihydrochloride trihydrate (2 mg/kg; labeled nuclei, Thermo Fisher Scientific, Eugene OR, USA), rhodamine 123 (5 μg/kg; labeled functional mitochondria in vivo, Thermo Fisher Scientific, Eugene OR, USA), and fluorescent rat albumin (for studies of glomerular permeability). Rat albumin (Sigma) was conjugated to Texas Red-X succinimidyl ester (AAT Bioquest, Sunnyvale, CA, USA) using standard procedures to achieve a final 1:1 protein-to-dye ratio and then extensively dialyzed using a 10 kDa cutoff filter before use (Sandoval et al., 2012). The preparation and validation of DL-594 conjugates of $G_4$1 mAb and $G_4$1-C-HC BfAb are described in the Results section. Immunofluorescence studies were conducted using rat anti-mouse F4/80 (Invitrogen, Carlsbad, CA, USA) and goat anti-mouse MMR (Macrophage Mannose/CD206 receptor, R&D systems, Minneapolis, MN, USA). Primary antibodies were fluorescently labeled using Alexa Fluor 488 goat anti-rat and Alexa Fluor 647 donkey anti-goat antibodies (Invitrogen, Carlsbad, CA, USA).

Intravital microscopy studies were conducted either 24 hours after intravenous injection of DL-594 conjugates $G_4$1-C-HC BfAb or $G_4$1 mAb (6.5 mg/kg) or during and for the first 2 hours following intravenous injection. Studies of mouse liver were conducted generally as described previously (Dunn and Day 2017; Ryan et al., 2018). Surgical preparation was started approximately 1 hour prior to imaging. The mouse was placed on an induction chamber connected to an anesthesia isoflurane circuit at 2% to 4% of isoflurane with 1% O_2. Once stabilized under anesthesia, the ventral abdominal side of the body and the right side of the neck were shaved and cleaned. Prior to exposing the liver, a jugular catheter was prepared for probe injections. A 1-cm right ventral incision was made in the neck, the jugular was exposed, and all fat and fascia surrounding were cleared. The anterior end of the jugular was tied using 4-0 silk suture to prevent bleeding. A tiny nick was made in the jugular vein, and a catheter was slid roughly 1 cm into the jugular vein and secured at the posterior end using 4-0 suture. The catheter was sutured and secured to the skin in three different places. After the jugular cannula was placed, the liver was exposed for imaging. A 2 × 2 cm piece of gauze moistened with saline was glued with a drop of cyanoacrylate to the skin just below the sternum. Exposure of the liver was begun with a 1-cm lateral ventral incision below the rib, and the skin and muscle layers were removed. The liver was then exposed by gently squeezing through the incision and placed on the moistened gauze. The liver was placed in a 40-mm covered glass-bottomed dish (WillCo Well) and glued to the cover glass without pressure. The mouse was then transferred to the microscope stage and placed on warming pads under a heat lamp to maintain body temperature at 35°C to 37°C, as monitored using a rectal probe thermometer. The microscope objective was also maintained at 37°C via an objective heater.

For studies of mouse or rat kidneys, a jugular catheter was placed as described previously in the text. Following jugular catheterization, a 1-cm lateral incision was made over the left kidney, followed by a 0.5-cm incision in the peritoneal muscle. The kidney was identified and pulled up through the skin opening. Once the kidney was exposed, the adrenal gland and the renal ligament were separated. The kidney was then placed in a 40-mm covered glass-bottomed dish with a 2 × 2 cm piece of gauze moistened with saline.

Intravital microscopy imaging studies were conducted using a Leica TCS SP8 DIVE confocal/multiphoton system mounted on an inverted stand. The imaging was performed using either 25X NA 0.95 water immersion or 63X NA1.3 glycerol immersion Leica HCX APO objective lenses. Images were collected using multiphoton fluorescence excitation at 800 nm. Three channels of fluorescence were collected in non-descanned detectors using emission bandpass filters of 405 to 450 nm (blue), 500 to 550 nm (green), and 600 to 650 nm (red). Image volumes were collected using 600 Hz bidirectional scanning at different zoom factors and a vertical spacing of 1.5 microns. Before imaging of the liver, mice were injected intravenously with Hoechst (2 mg/kg) to label nuclei. For studies of the early stages of antibody disposition, images were collected prior to, during, and every 20 minutes for 2 hours following intravenous injection of either $G_4$1 mAb or $G_4$1-C-HC BfAb (6.5 mg/kg). For studies of mice 24 hours after intravenous injection of antibodies, several image volumes and mosaics were collected following intravenous injection of Hoechst. In both sets of studies, mice were injected with rhodamine123 to verify the vitality of the liver (mitochondrial function). At the end of imaging, the mouse was perfuse-fixed, and liver tissue was collected. Intravital microscopy studies of the kidney were conducted similarly, with the exception that rhodamine123 was omitted, and in the case of rat studies, fluorescent albumin was injected at the times indicated.

Immunofluorescence Studies of Mouse Liver Sections. Immunofluorescence was conducted on mouse liver tissue following intravital microscopy. Tissue cut to a thickness of 50 microns was placed in blocking buffer (10% donkey serum, 0.1% Triton ×100 in PBS) for 3 hours and then incubated with anti-mouse F4/80 and anti-mMMR (1:50 in blocking buffer) in an orbital shaker at room temperature overnight. The following day, tissues were washed 4× in PBS and then incubated with Alexa Fluor 488 goat anti-rat and Alexa Fluor 647 donkey anti-goat (1:200 in blocking buffer) in an orbital shaker at room temperature overnight. The next day the tissue was washed 5× in PBS and post-fixed in 4% fresh paraformaldehyde for 10 minutes. The tissue was then rinsed 3× in PBS and mounted in Fluoromount aqueous mounting medium (Sigma). Image volumes were collected using confocal microscopy (Leica SP8 DIVE) and a Leica40X NA 1.3 oil immersion objective. Image volumes were collected over a range of zoom values, with an axial spacing of 0.7 microns.

Quantitative Image Analysis of Liver and Kidney Microscopy Data. Quantitative image analysis was conducted using Metamorph image processing software (Molecular Devices, Downington, PA, USA). Kidney endosome red–green fluorescence ratios were calculated by first subtracting the background from both the red and green channels (measured as the median intensity of a 64 × 64 region around each voxel) (Maxfield and Dunn, 1990) and then measuring the mean fluorescence of each channel in regions of interest drawn over three to nine proximal tubules. Liver punctate microvascular fluorescence was quantified by first subtracting the blue channel from the red channel for each image of the volume (to eliminate crosstalk of Hoechst fluorescence). Diffuse fluorescence (i.e., from freely circulating probes) was removed first by subtracting the median intensity of an 8 × 8 region from each voxel, followed by thresholding images to a value that eliminated residual diffuse fluorescence. Images of 17 focal planes from each three-dimensional volume were then summed, and fluorescence was then measured in each of four 400 × 400 voxel regions in the summed images. Images from all conditions were processed and quantified identically. Glomerular sieving coefficients were determined using our previously published method (Sandoval et al., 2012). A series of publications have described in detail the proper parameters to set the detector offset (black level), which is crucial for correctly detecting the low-intensity signal coming from fluorescent albumin in Bowman's space (Sandoval et al., 2012; Sandoval and Molitoris 2013; Dickson et al., 2014; Sandoval, Wang, and Molitoris 2014). Briefly, *z*-stack images of the glomerulus before fluorescent albumin infusion were collected to enable background fluorescent levels of Bowman's space and glomerular capillaries to be quantified. These values were subtracted from the same region after the fluorescent albumin infusion. Quantitative analyses were conducted using raw image data, but micrograph images

presented in figures were contrast-enhanced in a way that preserved the visibility of both the dim and bright structures of the original images. Images to be directly compared were contrast-enhanced identically. Images in figures were processed, assembled, and annotated using Adobe Photoshop. Graphs and summary statistics were generated using Kaleidagraph (Synergy Software, Reading, PA, USA).

Results

G_41 mAb and G_41-C-HC BfAb Model System. The studies described herein were performed using the G_41- mAb and G_41-C-HC BfAb molecules that were previously described (Datta-Mannan et al., 2019). The IgG_4-based G_41- mAb was developed against an undisclosed soluble target with no measurable concentrations in normal animals (Datta-Mannan et al., 2019). The G_41-C-HC BfAb has the D2 domain of VEGFR1, an approximately 11.5 kDa protein, as the ECD fusion partner, connected via a flexible glycine–serine linker to the C-terminal end of the HC of G_41 mAb (Supplemental Fig. 1). The ECD binds its soluble targets VEGF and PLGF and isoforms thereof, which are known to have low ng/ml and pg/ml circulating concentrations in the blood of normal animals, respectively (Molskness et al., 2004; Xin et al., 2012). The C-terminal HC position was selected for the fusion configuration of the ECD protein domain based on theoretically allowing the bispecific construct increased target binding accessibility such that the mAb could engage its targets concomitantly without steric hindrance. Mutations were made in both the Fc region of G_41- mAb to eliminate effector function and in the hinge region of G_41- mAb to remove any potential for in vivo arm exchange with endogenous IgGs (Labrijn et al., 2009; Silva et al., 2015; Labrijn et al., 2019). The mutations in the Fc and hinge regions were transitioned into the mAb component of the G_41-C-HC BfAb; thus, the only differences between the molecules are the peptide linker and ECD fusion within G_41-C-HC BfAb.

Tissue Distribution of Radiolabeled G_41 mAb and G_41-C-HC BfAb in Mice. A radiolabel biodistribution study of ^{111}In-labeled DTPA-conjugated versions of the G_41 mAb and G_41-C-HC BfAb molecules was conducted to evaluate the concentrations of the molecules at static time points (1, 6, 12, and 24 hours) following intravenous administration to mice. The goal of this study was to analyze the whole-body biodistribution of the G_41 mAb and G_41-C-HC BfAb in multiple tissues using traditional quantitative radiolabel methods to identify the tissues involved in clearance for subsequent dynamic intravital imaging disposition studies. Plasma and tissue concentrations of ^{111}In-labeled DTPA conjugates were measured over 24 hours following intravenous injection in CD-1 mice and reported as a percentage of the injected dose per gram of plasma or tissue.

The G_41 mAb and G_41-C-HC BfAb displayed similar plasma concentrations up to 24 hours post-administration, consistent with the exposure profiles for their respective unlabeled counterparts (Supplementary Fig. 2). Due to the sparse number of concentrations versus time plasma samples, PK parameters, such as clearance and half-life, were not determined. Tissue concentrations were measured 1, 6, 12, and 24 hours following intravenous administration. The vast majority of the constructs were detected in the liver, kidney, spleen, muscle, and skin, whose percent injected dose per gram (%ID/g) concentrations are reported in Fig. 1 (along with pooled measurements from the remaining tissues, listed as "other"). When the weight (grams) of the organs is considered, the highest concentrations were found in two organs of elimination, the liver and kidney, which were thus chosen as the focus of intravital microscopy studies.

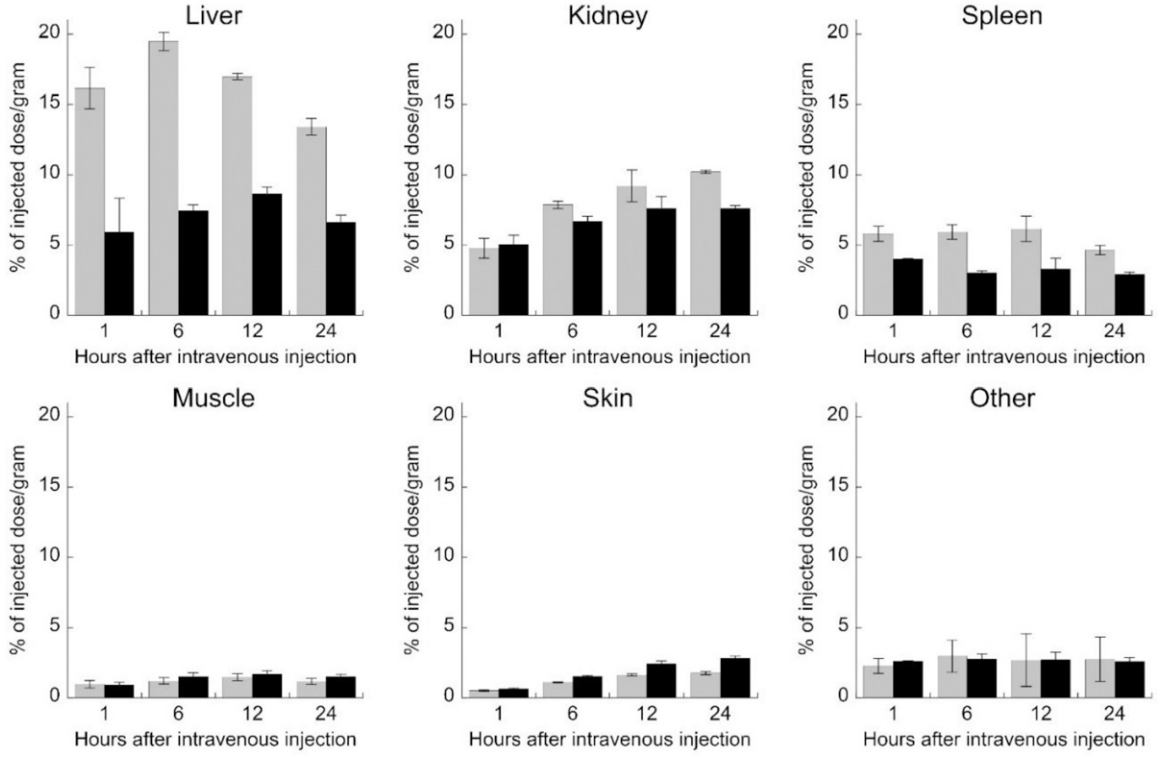

Fig. 1. Radiolabel biodistribution data for the mAb and BfAb in mice following a single intravenous administration of approximately 2 mg/kg (approximately 0.020 μCi/animal). Mean percentage of injected dose/g of tissue (±S.E.) of ^{111}In-DTPA-G_41 mAb (black columns) and ^{111}In-DTPA-G_41-C-HC BfAb (gray columns) determined by gamma counting radioactive signal. Data for the five organs that displayed the highest tissue concentrations are reported. The sum of the %ID/g for all additional organs collected are reported as "other."

Description and Physiochemical Characterization of the DL594 Fluorescently Labeled G_41 mAb and G_41-C-HC BfAb Molecules. As our dynamic disposition IVM studies are based upon the detection of fluorescently labeled molecules, we conjugated G_41-mAb and G_41-C-HC BfAb with DL594 at a ratio of one to two fluorophore molecules per antibody. Since conjugation of mAbs with fluorescent dyes has sometimes been found to alter their physiochemical properties (Cilliers et al., 2017) in ways that might influence in vivo disposition, we conducted physiochemical characterizations of the fluorescent conjugates with respect to properties that have been shown to influence clearance in vivo (Igawa et al., 2010; Boswell et al., 2010; Hotzel et al., 2012; Datta-Mannan et al., 2012; Datta-Mannan and Wroblewski 2014; Datta-Mannan et al., 2015). The results of these analyses are summarized in Table 1.

A previously developed heparin-based column assay was used to determine the degree of charge-based interaction for the DL594-labeled molecules relative to their respective unlabeled counterparts (Datta-Mannan et al., 2020). In this experiment, the molecules were injected over a column of heparin sepharose and then eluted with a linear gradient of increasing ionic strength. Neither DL594-labeled nor DL594-unlabeled G_41-C-HC BfAbs showed retention on the heparin column, indicating the DL594 labeling did not affect the overall electrostatic properties (Table 1).

Changes in nonspecific interactions of the molecules as a consequence of DL594 labeling driven by hydrophobic association were evaluated using a HIC-based high-performance liquid chromatography assay in which molecules were injected onto a solid-phase hydrophobic resin pre-equilibrated in high concentrations of salt. DL594 labeling led to a similar shift to becoming more hydrophobic (i.e., longer elution time and higher %HIP) for both molecules evaluated. This was not unexpected given the solvent-accessible nature of the aromatic-based dye additions to the mAb or BfAb and the relative consistency in retention time shifts were congruent with the similar dye-to-protein ratio for each molecule (Table 1).

Binding of the DL594-labeled G_41-mAb and G_41-C-HC BfAb to FcRn was measured using a previously reported microscale thermophoresis method (Wagner et al., 2016). Results of these studies show that the two molecules bind to rat FcRn with similar affinities and that conjugation to DL594 did not significantly alter either the weak or strong affinities of either, indicating a conserved engagement profile with FcRn (Table 1).

Exposure of the DL594 Fluorescently Labeled G_41 mAb and G_41-C-HC BfAb Molecules in Rats After a Single Intravenous Administration. Others have reported that labeling of mAbs with fluorescent dyes can alter their exposure, thus potentially confounding the evaluation of their tissue and cellular disposition profiles (Cilliers et al., 2017). Therefore, we compared the exposures of the DL594-labeled and their unlabeled counterpart G_41 mAb and G_41-C-HC BfAb in rats up to the latest time point to be evaluated by IVM (approximately 24 hours post-administration) to evaluate the influence of the fluorescent dye conjugation on the behavior of the molecules. Rats were selected for these studies as serial blood sampling is relatively less invasive than in mice. Following a single 1 mg/kg intravenous administration of each construct, the mean exposures of the DL594-labeled G_41 mAb and G_41-C-HC BfAb and their respective unlabeled molecules were similar in rats up to 24 hours post-administration (Supplementary Fig. 3), indicating that conjugation of the molecules did not change their in vivo behavior. In addition, the DL594-conjugated G_41 mAb and G_41-C-HC showed similar blood concentrations up to 24 hours post-dose, consistent with previous findings in rodents (Supplementary Fig. 3C) (Datta-Mannan et al., 2019). Divergence of the PK profiles of the DL594-conjugated molecules became evident in the elimination phase (i.e., post 24 hours following administration) (Supplementary Fig. 3D) and resulted in the DL594-labeled G_41-C-HC BfAb and DL594-labeled G_41 mAb displaying a clearance of approximately 1.8 ml/h/kg and approximately 1.0 ml/h/kg, respectively (Table 2). The approximately twofold more rapid clearance observed for DL594-labeled G_41-C-HC BfAb relative to G_41-DL594 is consistent with the PK reported in previous studies for the unlabeled counterparts in mice (Datta-Mannan et al., 2019).

Intravital Microscopy Studies of the Disposition of DL594-Labeled G_41 mAb and G_41-C-HC BfAb in Mouse Liver. Intravital microscopy studies of the liver disposition of the DL594-labeled G_41 mAb and G_41-C-HC BfAb constructs in mice were conducted approximately 1 and 24 hours following a single intravenous dose of each construct (Fig. 2). Both constructs were found to accumulate in puncta on the boundaries of the liver capillaries throughout the sinusoid network, although with different kinetics. Whereas the fluorescence of G_41-C-HC puncta increased to high levels within the first hour, G_41-C-HC BfAb puncta were relatively dim 1 hour after administration but accumulated to levels similar to those of G_41-C-HC over 24 hours. The puncta are more easily appreciated in high-magnification images (Fig. 2, E–H). To better delineate hepatocytes, mice were also injected with rhodamine123, a green-fluorescing probe that accumulates in active mitochondria and strongly labels hepatocytes in vivo. These and subsequent figures demonstrate that neither compound appears to associate with hepatocytes.

To characterize the dynamics of the accumulation of the G_41 mAb and G_41-C-HC BfAb molecules in sinusoid puncta, studies were conducted in which the same regions of the liver were repeatedly imaged over an approximately 2-hour period immediately following intravenous injection. As shown in Fig. 3A, fluorescent puncta can be detected in sinusoids within 19 minutes of injection of the G_41-C-HC BfAb, and the fluorescence of these puncta increases with time, particularly during the next 30 minutes. Similar results were obtained in mice injected with G_41 mAb that, within 11 minutes of injection, could be detected in distinct puncta that subsequently increased in fluorescence over the next hour (Fig. 3B). Quantitative analysis of the integrated fluorescence of punctate of G_41 mAb and G_41-C-HC BfAb measured in replicate mice approximately 1 and 24 hours after injection demonstrate that G_41 mAb accumulates more than 2× faster than G_41-C-HC BfAb during the

TABLE 1

Properties of the molecules

Molecule	Heparin binding [(NaCl) at main peak elution apex, mM]	HIC chromatography		Rat FcRn binding K_D (μM)
		Retention time (min)	%HIP	
G_41 mAb	None	10.3	36.1	2.1
G_41 mAb-DL594	None	12.1	43.9	1.8
G_41-C-HC BfAb	None	14.7	55.2	4.0
G_41-C-HC BfAb–DL594	None	16.0	60.9	4.1

TABLE 2

Mean (± S.D.) PK parameters of the molecules
n = 3 rats/time point. All PK parameters were determined from noncompartmental PK analyses unless otherwise noted.

Molecule	C_{max} (μg/ml)	$AUC_{0-\infty}$ (h* μg/ml)	CL (ml/h/kg)	$T_{1/2}$ (h)	V_{ss} (ml/kg)
G_41 mAb–DL594	39.8 (3.0)	1019 (180)	1.00 (0.19)	15.2 (2.7)	27.8 (5.5)
G_41-C-HC BfAb–DL594	39.4 (3.6)	585 (35)	1.81 (0.10)	24.9 (2.5)	26.1 (2.6)

C_{max}, maximal observed serum concentration; $AUC_{0-\infty}$, area under the plasma concentration curve from time zero extrapolated to infinite time; CL, clearance; $T_{1/2}$, elimination half-life.

first hour. However, G_41-C-HC BfAb continues to accumulate, finally achieving comparable levels within 24 hours (Fig. 3C).

Comparisons of fields collected 1 hour with those collected 24 hours after injection demonstrated that whereas the integrated fluorescence of punctate G_41 mAb increased insignificantly (approximately 1.7-fold between 1 and 24 hours), the integrated fluorescence of punctate G_41-C-HC BfAb increased more than fourfold over the same period ($P = 0.001$).

The studies shown in Fig. 3 were conducted in Lys-EGFP mice, which express EGFP under control of the lysozyme promoter (Faust et al., 2000). While EGFP is expressed by all myelomonocytic cells, it is expressed most strongly in neutrophils, which are indicated with arrows. A close comparison of the indicated cells in the green and red channels suggests that only modest amounts of G_41 mAb and G_41-C-HC BfAb associate with neutrophils immediately following intravenous injection. Additional studies, conducted to characterize the nature of the structures in which G_41 mAb and G_41-C-HC BfAb accumulate and to identify the cells in which they accumulate, are described in the following text.

Images collected from living mice at higher resolution (Fig. 4) indicate that the G_41 mAb and G_41-C-HC BfAb constructs are internalized by the endothelial cells lining the liver sinusoids. Figure 4A shows an example of a field collected from the liver 24 hours after intravenous injection of the G_41-C-HC BfAb. Numerous endothelial nuclei can be found throughout the field, each surrounded by a ring of punctate G_41-C-HC BfAb fluorescence. The close apposition of the puncta with nuclei in the same focal plane suggests that the G_41-C-HC BfAb punctate fluorescence derives from intracellular compartments, likely endothelial

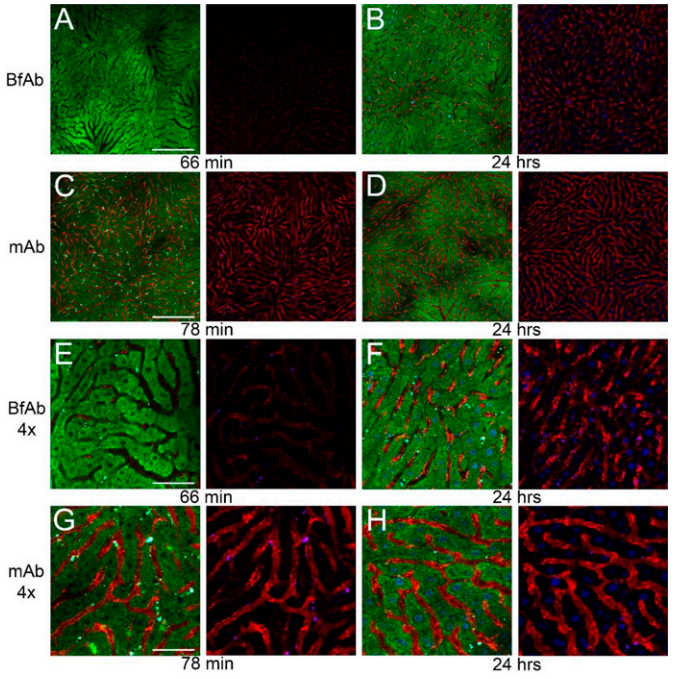

Fig. 2. Intravital microscopy of mouse liver following intravenous injection of G_41-C-HC-DL594 BfAb or G_41-DL594 mAb. Low-power images of the liver of a living mouse collected 66 minutes (A) and 24 hours (B) after intravenous injection of 6.5 mg/kg G_41-C-HC-DL594 BfAb. Red: DL594; blue: Hoechst 33342 (nuclei); green: rhodamine123, a fluoresent probe that accumulates in actively respiring mitochondria, particularly in hepatocytes in vivo. C and D are corresponding images collected 78 minutes (C) and 24 hours (D) after intravenous injection of G_41-DL594 mAb. E and F are 4× magnified regions from panels A and B, respectively. G and H are 4× magnified regions from panels E and F, respectively. Scale bars represent 200 microns for low-power images and 50 microns for high-power images.

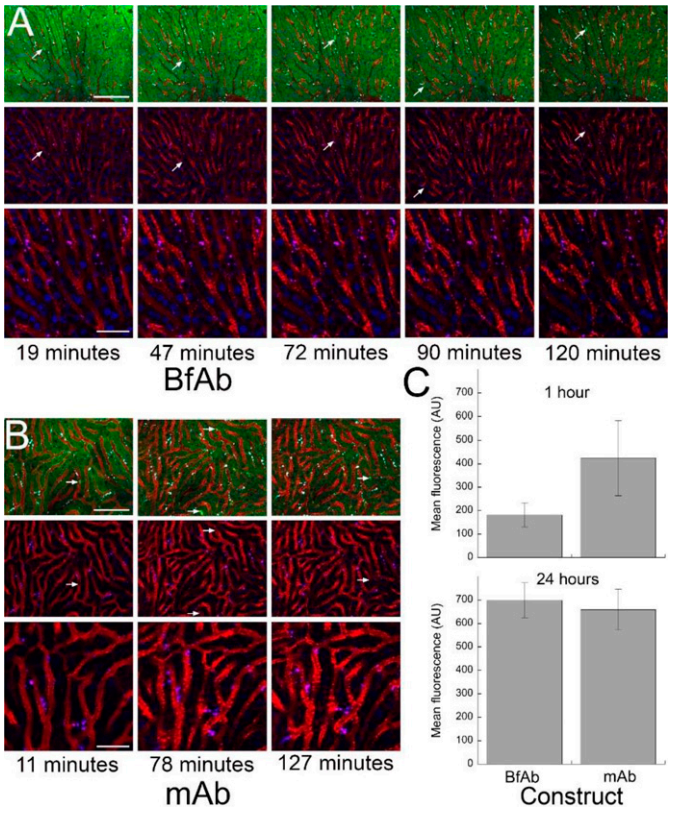

Fig. 3. Accumulation of G_41-C-HC-DL594 BfAb or G_41-DL594 mAb in the liver vasculature of Lys-EGFP mice. (A) Series of images collected from the liver of a living mouse over the 2-hour period following intravenous injection of 6.5 mg/kg G_41-C-HC-DL594 BfAb (red). As in Fig. 3, the blue signal derives from the nuclear probe Hoechst 33342, and the green signal derives from rhodamine123, which strongly labels hepatocytes in vivo. First row – all probes. Second row – Hoechst 33342 and G_41-C-HC-DL594 BfAb (red). Third row – as in the second row but magnified 2 times. (B) A series of images collected from the liver of a living mouse over the 2-hour period following intravenous injection of G_41-C-HC-DL594 BfAb. First row – all probes. Second row – Hoechst 33342 and G_41-C-HC-DL594 BfAb (red). Third row – as in the second row but magnified 2 times. (C) Results of quantification of field-wise fluorescence of G_41-C-HC-DL594 BfAb or G_41-DL594 mAb 1 hour (top) or 24 hours (bottom) after injection. Graphs indicate means and S.E. of analyses of four mice injected with G_41-C-HC-DL594 BfAb and three mice injected with G_41-DL594 mAb. Scale bars represent 100 microns for low-power images and 40 microns for high-power images.

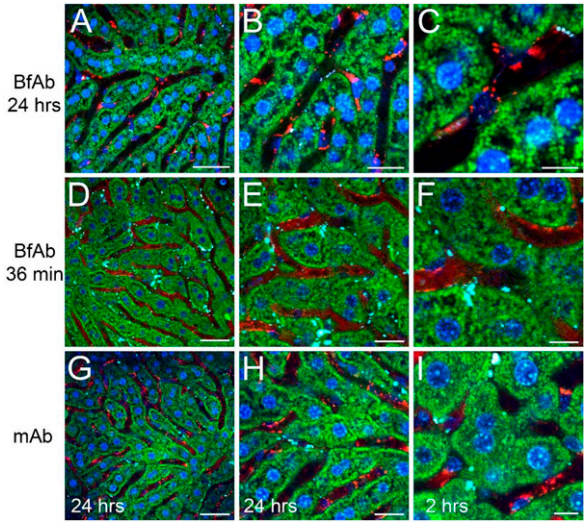

Fig. 4. Accumulation of G_41-C-HC-DL594 BfAb or G_41-DL594 mAb in sinusoidal endothelia in mouse liver. (A) Image collected from the liver of a living mouse 24 hours after intravenous injection of 6.5 mg/kg G_41-C-HC-DL594 BfAb (red). (B) 2× magnified region of the image shown in panel A. (C) Image collected at higher resolution from the same field. As in Fig. 3, the blue signal derives from the nuclear probe Hoechst 33342, and the green signal derives from rhodamine123, which are clearly resolved in these high-resolution images. (D) Image collected from the liver of a living mouse 36 minutes after intravenous injection of 6.5 mg/kg G_41-C-HC-DL594 BfAb (red). (E, F) 2× and 4× magnified regions, respectively, of the image shown in panel D. (G) Image collected from the liver of a living mouse 24 hours after intravenous injection of 6.5 mg/kg G_41-DL594 mAb (red). (H) 2× magnified region of the image shown in panel G. (I) Image collected from the mouse 2 hours after intravenous injection of 6.5 mg/kg G_41-DL594 mAb. Scale bars represent 40 microns (A, D, and G), 20 microns (B, E, and H) and 10 microns (C, F, and I)

endosomes. The apposition of these puncta with endothelial nuclei is even more obvious in the magnified region of the image (Fig. 4B) and in the image collected from a different focal plane from the same field (Fig. 4C). These apparently internal structures are evident even as early as 36 minutes after injection (Fig. 4, D–F), although they are somewhat less obvious against the background of free G_41-C-HC BfAb in the plasma at this early time point. Similar results were obtained in studies of the disposition of the G_41 mAb. As with G_41-C-HC BfAb, the G_41 mAb is also found surrounding endothelial nuclei both at 24 hours (Fig. 4, G and H) and 2 hours after injection (Fig. 4I). These results are consistent with endocytic uptake and accumulation of G_41-C-HC BfAb and G_41 mAb in the sinusoidal endothelia of the mouse liver.

Consistent with the images collected at early time points shown in Fig. 3, images collected 24 hours after injection demonstrate that only a minor fraction of the accumulated G_41 mAb and G_41-C-HC BfAb molecules associate with EGFP-expressing neutrophils in EGFP-Lys mice (Supplementary Fig. 4). To more definitively identify the cells internalizing G_41 mAb and G_41-C-HC BfAb, we conducted immunofluorescence studies in which tissues were labeled with antibodies to CD206, a marker of liver endothelia, and F4/80, a marker of Kupffer cells. Consistent with the results shown in Supplementary Fig. 4, studies of liver tissues fixed 24 hours after intravenous injection demonstrate that the G_41-C-HC BfAb accumulation closely corresponds to CD206-positive cells, consistent with internalization by endothelial cells (Supplementary Fig. 5, A and B). Since CD206 is also expressed at low levels by Kupffer cells, additional studies were conducted in tissues labeled with antibodies against both CD206 and F4/80 (Supplementary Fig. 5C). As with the images shown in Supplementary Fig. 5, A and B, these images show that G_41-C-HC BfAb associates with cells labeled with CD206 but not with cells labeled with F4/80. Similar results were obtained in studies of liver tissues of mice 24 hours after injection with G_41 mAb, whose distribution closely corresponded with cells expressing CD206, but not with cells expressing F4/80 (Supplementary Fig. 5, D and E, respectively).

Intravital Microscopy Studies of the Disposition of DL594-Labeled G_41 mAb and G_41-C-HC BfAb in Mouse Kidney. Intravital microscopy studies were next conducted on the kidney, the second major organ in which the constructs accumulated. Figure 5 shows images collected from the kidney of living C57BL/6 mice following intravenous injection of DL594 fluorescent conjugated G_41-C-HC BfAb (Fig. 5, A–D) or G_41 mAb (Fig. 5, E–H) at various times after administration. Neither compound was found to accumulate in detectible structures during the first 70 minutes, instead remaining apparently free in the vascular circulation. However, over the next 24 hours, DL594-G_41-C-HC BfAb accumulated to very high levels in what appear to be endosomes and/or lysosomes of proximal tubule cells. No comparable accumulation was found in mice injected with DL594-G_4 1 mAb, which appeared to remain free in the vascular circulation.

Similar results were obtained in intravital microscopy studies of the kidney of Munich–Wistar rats. As observed in the murine kidney IVM studies, both G_41 mAb and G_41-C-HC BfAb are largely retained in the plasma for at least the first hour after injection (Fig. 6, A and D). However, over the next 24 hours, the distribution of G_41-C-HC BfAb dramatically changes, diminishing in the plasma and increasing dramatically in endosomes of the proximal tubule epithelia, as evidenced in the shift in the spectrum of their fluorescence from the yellow characteristic of endogenous lysosomal autofluorescence to red (Fig. 6, B

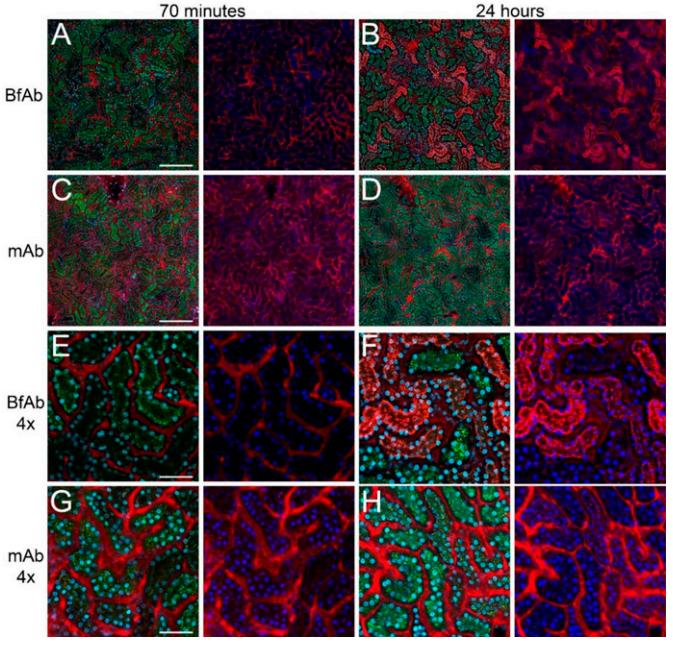

Fig. 5. Intravital microscopy of mouse kidney following intravenous injection of G_4 1-C-HC-DL594 BfAb or G_41-DL594 mAb. (A) Low-power image of the kidney of a living mouse collected 75 minutes after intravenous injection of 6.5 mg/kg G_41-C-HC-DL594 BfAb (red). The green signal derives from tissue autofluorescence, and the blue signal derives from the fluorescence of the nuclear probe Hoechst 33342 introduced 30 minutes prior to G_41-C-HC-DL594 BfAb injection. (B) Low-power image of the kidney of a living mouse collected 24 hours after intravenous injection of G_41-C-HC-DL594 BfAb. (C, D) Corresponding high-power images collected at 75 minutes and 24 hours, respectively. (E) Low-power image of the kidney of a living mouse collected 75 minutes after intravenous injection of 6.5 mg/kg G_41-C-HC-DL594 mAb (red). (F) Low-power image of the kidney of a living mouse collected 24 hours after intravenous injection of G_41-C-HC-DL594 mAb. (G, H) Corresponding high-power images collected at 75 minutes and 24 hours, respectively. Scale bars represent 200 microns for low-power images and 50 microns for high-power images.

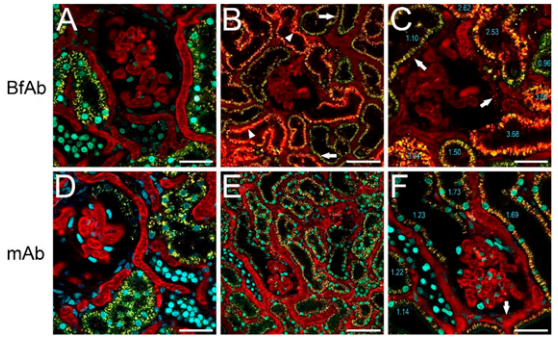

Fig. 6. Intravital microscopy of rat kidney following intravenous injection of G_41-C-HC-DL594 BfAb or G_41-DL594 mAb. (A) Image of the kidney of a living Munich Wistar Fromter rat collected 66 minutes after intravenous injection of 6.5 mg/kg DL594-G_41-C-HC BfAb (red). The green signal derives from tissue autofluorescence, and the blue signal derives from the fluorescence of the nuclear probe Hoechst 33342 introduced 30 minutes prior to G_41-C-HC-DL594 BfAb injection. (B) Low-power image of the kidney of a living rat collected 24 hours after intravenous injection of G_41-C-HC-DL594 BfAb. (C) 2× magnified image collected from the same field shown in B. (D) High-power image collected from a different region of the kidney shown in panels A to C. (E) Image of the kidney of a living rat collected 63 minutes after intravenous injection of 6.5 mg/kg G_41-DL594 mAb (red). (F, G, and H) Images collected at different magnifications, from different focal planes from the kidney of a living rat 16 hours after intravenous injection of G_41-DL594 mAb. Values shown in panels C and G represent mean red-to-green fluorescence ratios of the different tubules. Scale bars represent 40 microns (A, C, E, and G), 80 microns (B and F) and 20 microns (D and H).

and C). Quantifications of the red-to-green fluorescence ratio in each tubule demonstrate that the ratio shifts from an initial mean of 0.95 measured 1 hour after injection to values 24 hours later as high as 3.68 (Fig. 6C). In contrast, and consistent with observations in mice, the distribution of G_41 mAb on the day following injection (approximately 24 hours post-administration) is essentially identical to that at 1 hour, with only a minor decrease in vascular levels and a modest shift in the spectrum of endosome/lysosome fluorescence (Fig. 6, E and F).

The presence of G_41-C-HC BfAb in proximal tubule endosomes in both mice and rats indicates that while not filtered rapidly enough to be visually apparent in Bowman's space, it is nonetheless filtered to some degree. Because the glomeruli of Munich–Wistar rats occur at depths that are accessible to microscopy, it was possible to quantify the glomerular permeability of the two constructs (Sandoval and Molitoris 2013). Consistent with the visual observations, quantifications of glomerular sieving coefficients (see the Methods section) demonstrate that both are minimally filtered, with glomerular sieving coefficients of 0.00685 ± 0.00018 for G_41-C-HC BfAb and 0.00532 ± 0.00071 for G_4 1 mAb.

Discussion

The studies described here were predicated on the observation that the rate of peripheral clearance of G_41-C-HC BfAb was roughly double that of the parent G_41 mAb. This difference was unexpected since G_41-C-HC BfAb was specifically designed to minimize physiologic interactions known to influence the PK of biologics (Tibbitts et al., 2016; Datta-Mannan, 2019). For instance, while the G_41-C-HC BfAb was constructed with an ECD (the D2 domain VEFGR1) fused to the HC C-terminus of the G_41 parental mAb, the ECD and mAb targeted two distinct soluble ligands that have negligible peripheral concentrations in normal animals (Molskness et al., 2004; Xin et al., 2012). Moreover, the BfAb had no specific interaction with cell surface receptors, thus eliminating both circulating ligand-mediated and cell surface target-mediated drug disposition as potential mechanisms for the observed clearance. In addition, since the G_41-C-HC BfAb used the same IgG_4 parental Fc within G_41 mAb that has been engineered to eliminate interactions with Fcγ receptors, direct binding with blood cells is not expected to be a major viable clearance mechanism either (Shields et al., 2001). The fact that the two used the same Fc region and showed similar in vitro FcRn interaction properties also argues that the difference in clearance was not based upon differences in interactions with FcRn in vivo, as has been observed for other antibody modalities (Datta-Mannan and Wroblewski 2014; Pyzik et al., 2015). Although native IgG_4-based antibodies have a strong potential for Fab-arm exchange with endogenous IgG4s that can lead to aberrant and suboptimal PK properties (Labrijn et al., 2009; Silva et al., 2015), the inclusion of the S228P mutation in the hinge region of the G_41 mAb and G_41-C-HC BfAb eliminated this potential and, thereby, also excluded IgG_4-related hinge instability differential as a plausible mechanism for the PK differences.

Radiolabeled disposition and intravital microscopy studies were thus conducted to characterize the tissue and cellular interactions of the G_41-C-HC BfAb construct, which despite being engineered for minimal off-target cellular interactions, cleared twofold faster from the peripheral circulation in mice and rats. Whole-body biodistribution studies demonstrated that the two constructs accumulated to similar degrees in most tissues except for the liver, in which G_41-C-HC BfAb accumulated to approximately two- to threefold higher concentrations. This difference was apparent within the first hour of administration but was maintained throughout the 24-hour time course of the study (Fig. 1). The fact that levels of the two in the plasma were essentially superimposable over this period (Supplementary Fig. 2A) clearly shows that the G_41-C-HC BfAb has higher mean liver:blood accumulation relative to the G_41 mAb, suggesting G_41-C-HC BfAb has a strong liver-binding component at early time points that may contribute to its faster peripheral clearance relative to the G_41 mAb.

Intravital microscopy studies identified profound differences between the cellular interactions of the two molecules. Both constructs were found to accumulate in endosomes of the sinusoidal endothelia of the liver but with different kinetics. In contrast to the results of the radiolabel studies, the fluorescent probe DL594-G_41 mAb was found to accumulate more than 2× faster than DL-G_41-C-HC BfAb during the first hour, after which time DL-G_41-C-HC BfAb continues to accumulate, finally achieving similar levels by 24 hours (Fig. 3). The basis for the discrepancy with the results of the radiolabel studies may reflect differences in the residualizing properties of Lys-DTPA-^{111}In used in the radiolabel studies versus the DL594 used in the IVM studies. Insofar as IVM demonstrated that both compounds were internalized into the endolysosomal system of endothelia, these differences are likely to be important. To our knowledge, the residualizing properties of probes labeled with fluorescent probe DL594 have not been published. However, they are almost certainly different from those labeled with the residualizing agent DTPA-^{111}In. This is because DTPA-^{111}In retains its cellular localization even after degradation of the parent conjugate; thus, its abundance will reflect the abundance of both the intact and degraded conjugate. In contrast, fluorescent probes such as DL594 are free to disperse and diffuse out of cells following the degradation of the antibody conjugate. As such, the DL594 fluorescence will more closely reflect just the levels of the intact conjugate at the particular time point of imaging. To the degree that some extent of conjugate degradation occurs in endosomal compartments, which include lysosomes, the amount of conjugate that has been directed to these compartments will be more accurately reflected by levels of DTPA-^{111}In whereas it will be underrepresented by the levels of DL594 fluorescence. It is tempting to speculate that the combined data suggest that the accelerated peripheral clearance BfAb reflects

degradation due to increased partitioning to a degradative endocytic pathway in liver sinusoidal endothelia.

Although radiolabel distribution studies indicated no differences in how mAb and BfAb interact with the kidney (Fig. 1), IVM studies of rats and mice identified profound differences between the two (Figs. 5 and 6). While both were observed only free in the plasma flowing through the peritubular capillaries within 1 hour of administration, BfAb accumulated dramatically in endosomes of the proximal tubule over 24 hours. The accumulation of BfAb, but not mAb, in proximal tubule endosomes was somewhat unexpected. Although both visual and quantitative analyses indicated minimal glomerular permeability of either compound in our studies, previous studies have demonstrated that limited amounts of IgG are filtered in the mouse kidney and internalized into endosomes of the proximal tubule (Lawrence et al., 2017). However, one would expect the levels of BfAb in proximal tubule endosomes to be less, rather than more, than those of mAb simply due to its larger size and thus lower glomerular permeability. The pronounced accumulation of BfAb over 24 hours was likewise unexpected since it is believed the IgGs are transcytosed back into the circulation following internalization by the proximal tubule, rather than accumulating (Kobayashi et al., 2002; Lawrence et al., 2017). One possible explanation is that the strong endosomal fluorescence observed 24 hours after administration of DL594-BfAb derives from fluorescently labeled fragments of the degraded compound, generated in liver endothelia as described in the previous text. This provides a satisfying explanation for the much stronger endosomal fluorescence observed in mice 24 hours after injection with DL594-BfAb, whose degradation would result in the continuous generation of fragments that would be freely filtered and internalized by proximal tubule cells. To the degree that the distribution of fluorescent fragments differs from that of the residualizing Lys-DTPA-^{111} In probe, this model might also explain the discrepancy between the IVM studies and the radiolabel studies, which detected no difference in the accumulation of the two probes in the kidney.

Another possible explanation for the observation of the accumulation of DL594-BfAb, but not DL594-mAb, in proximal tubule endosomes is that while both are filtered and internalized into proximal tubule cells, their subsequent intracellular fates are different. As described in the previous text, IgGs internalized into proximal tubule cells are believed to be directed onto a transcytotic pathway for return to circulation. Accordingly, the steady-state levels of mAb associated with proximal tubule cells would be expected to be limited by the continuous transcytotic efflux. In contrast, if the molecular modifications of BfAb altered its interactions with the endocytic sorting machinery involved in transcytosis, it would be expected to accumulate on a lysosomal pathway.

The molecular basis for the differences in the cellular interactions of the two compounds is unclear. As described in the previous text, the BfAb was specifically designed to avoid off-target cellular interactions. Physicochemical analyses revealed only a subtly enhanced propensity of the G_41-C-HC BfAb for hydrophobic-related interactions. Increased nonspecific binding potential, including those driven by electrostatic (i.e., charge) and hydrophobic interactions, have been empirically connected to PK behavior (Boswell et al., 2010; Igawa et al., 2010; Datta-Mannan et al., 2015, 2020; Jain et al., 2017; Hu and D'Argenio 2020; Grinshpun et al., 2021); thus, it seems reasonable to speculate that the increased propensity of G_41-C-HC BfAb for hydrophobic interactions may have altered its interactions with surface receptors mediating endocytosis or with the molecular machinery mediating endocytic sorting leading to increased clearance relative to the mAb.

Alternatively, the differences in the disposition of the two compounds may reflect differences in their interaction with FcRn. While the FcRn binding affinity of G_41-C-HC BfAb at pH 6.0 was only modestly lower than that of G_41 mAb, it is intriguing to speculate that subtle differences in affinity, particularly in the context of the sequence of pH and physical environments experienced in vivo may underlie the observed differences in the in vivo disposition of BfAb and mAb. FcRn has a well-described role in preventing lysosomal degradation of IgG, mediating sorting of IgG onto a recycling pathway in endothelia and a transcytotic pathway in proximal tubule cells (Kobayashi et al., 2002; Roopenian and Akilesh 2007). Thus, while speculative, a model based on altered interactions with FcRn provides a unifying explanation that is consistent with the results of our IVM and radiolabel distribution studies and with the contention that the faster peripheral clearance of BfAb is based upon enhanced degradation of BfAb in liver endothelia and kidney proximal tubule epithelia.

In sum, the studies here demonstrate how the spatiotemporal resolution of IVM can be leveraged to expand our understanding of the in vivo disposition of therapeutics, detecting off-target interactions that could not be detected by conventional PK approaches or predicted by conventional physicochemical analyses.

Acknowledgments

The authors are grateful to Bernice Ellis and Linda Schirtzinger for their thoughtful discussions and technical contributions.

Authorship Contributions

Participated in research design: Datta-Mannan, Molitoris, Feng, Dunn.
Conducted experiments: Martinez, Sandoval, Brown, Merkel.
Contributed new reagents or analytic tools: Croy.
Performed data analysis: Martinez, Sandoval, Brown, Merkel.
Wrote or contributed to the writing of the manuscript: Datta-Mannan, Molitoris, Feng, Dunn.

References

Boswell CA, Bumbaca D, Fielder PJ, and Khawli LA (2012) Compartmental tissue distribution of antibody therapeutics: experimental approaches and interpretations. *AAPS J* **14:**612–618.
Boswell CA, Mundo EE, Firestein R, Zhang C, Mao W, Gill H, Young C, Ljumanovic N, Stainton S, Ulufatu S, et al. (2013) An integrated approach to identify normal tissue expression of targets for antibody-drug conjugates: case study of TENB2. *Br J Pharmacol* **168:**445–457.
Boswell CA, Yadav DB, Mundo EE, Yu SF, Lacap JA, Fourie-O'Donohue A, Kozak KR, Ferl GZ, Zhang C, Ho J, et al. (2019) Biodistribution and efficacy of an anti-TENB2 antibody-drug conjugate in a patient-derived model of prostate cancer. *Oncotarget* **10:**6234–6244.
Boswell CA, Tesar DB, Mukhyala K, Theil F-P, Fielder PJ, and Khawli LA (2010) Effects of charge on antibody tissue distribution and pharmacokinetics. *Bioconjug Chem* **21:**2153–2163.
Cilliers C, Nessler I, Christodolu N, and Thurber GM (2017) Tracking antibody distribution with near-infrared fluorescent dyes: impact of dye structure and degree of labeling on plasma clearance. *Mol Pharm* **14:**1623–1633.
Datta-Mannan A, Croy JE, Schirtzinger L, Torgerson S, Breyer M, and Wroblewski VJ (2016) Aberrant bispecific antibody pharmacokinetics linked to liver sinusoidal endothelium clearance mechanism in cynomolgus monkeys. *MAbs* **8:**969–982.
Datta-Mannan A (2019) Mechanisms influencing the pharmacokinetics and disposition of monoclonal antibodies and peptides. *Drug Metab Dispos* **47:**1100–1110.
Datta-Mannan A, Brown R, Key S, Cain P, and Feng Y (2021) Pharmacokinetic developability and disposition profiles of bispecific antibodies: a case study with two molecules. *Antibodies (Basel)* **11:**2.
Datta-Mannan A, Brown RM, Fitchett J, Heng AR, Balasubramaniam D, Pereira J, and Croy JE (2019) Modulation of the biophysical properties of bifunctional antibodies as a strategy for mitigating poor pharmacokinetics. *Biochemistry* **58:**3116–3132.
Datta-Mannan A, Chow CK, Dickinson C, Driver D, Lu J, Witcher DR, and Wroblewski VJ (2012) FcRn affinity-pharmacokinetic relationship of five human IgG4 antibodies engineered for improved in vitro FcRn binding properties in cynomolgus monkeys. *Drug Metab Dispos* **40:**1545–1555.
Datta-Mannan A, Estwick S, Zhou C, Choi H, Douglass NE, Witcher DR, Lu J, Beidler C, and Millican R (2020) Influence of physiochemical properties on the subcutaneous absorption and bioavailability of monoclonal antibodies. *MAbs* **12:**1770028.
Datta-Mannan A, Thangaraju A, Leung D, Tang Y, Witcher DR, Lu J, and Wroblewski VJ (2015) Balancing charge in the complementarity-determining regions of humanized mAbs without affecting pI reduces non-specific binding and improves the pharmacokinetics. *MAbs* **7:**483–493.
Datta-Mannan A and Wroblewski VJ (2014) Application of FcRn binding assays to guide mAb development. *Drug Metab Dispos* **42:**1867–1872.
Dickson LE, Wagner MC, Sandoval RM, and Molitoris BA (2014) The proximal tubule and albuminuria: really! *J Am Soc Nephrol* **25:**443–453.
Dunn KW and Day RN (2017) Imaging cell biology and physiology in vivo using intravital microscopy. *Methods* **128:**1–2.
Faust N, Varas F, Kelly LM, Heck S, and Graf T (2000) Insertion of enhanced green fluorescent protein into the lysozyme gene creates mice with green fluorescent granulocytes and macrophages. *Blood* **96:**719–726.

Grinshpun B, Thorsteinson N, Pereira JN, Rippmann F, Nannemann D, Sood VD, and Fomekong Nanfack Y (2021) Identifying biophysical assays and *in silico* properties that enrich for slow clearance in clinical-stage therapeutic antibodies. *MAbs* **13:**1932230.

Hötzel I, Theil FP, Bernstein LJ, Prabhu S, Deng R, Quintana L, Lutman J, Sibia R, Chan P, Bumbaca D, et al. (2012) A strategy for risk mitigation of antibodies with fast clearance. *MAbs* **4:**753–760.

Hu S and D'Argenio DZ (2020) Predicting monoclonal antibody pharmacokinetics following subcutaneous administration via whole-body physiologically-based modeling. *J Pharmacokinet Pharmacodyn* **47:**385–409.

Igawa T, Tsunoda H, Tachibana T, Maeda A, Mimoto F, Moriyama C, Nanami M, Sekimori Y, Nabuchi Y, Aso Y, et al. (2010) Reduced elimination of IgG antibodies by engineering the variable region. *Protein Eng Des Sel* **23:**385–392.

Jain T, Sun T, Durand S, Hall A, Houston NR, Nett JH, Sharkey B, Bobrowicz B, Caffry I, Yu Y, et al. (2017) Biophysical properties of the clinical-stage antibody landscape. *Proc Natl Acad Sci USA* **114:**944–949.

Khawli LA, Glasky MS, Alauddin MM, and Epstein AL (1996) Improved tumor localization and radioimaging with chemically modified monoclonal antibodies. *Cancer Biother Radiopharm* **11:**203–215.

Khawli LA, Goswami S, Hutchinson R, Kwong ZW, Yang J, Wang X, Yao Z, Sreedhara A, Cano T, Tesar D, et al. (2010) Charge variants in IgG1: isolation, characterization, in vitro binding properties and pharmacokinetics in rats. *MAbs* **2:**613–624.

Kobayashi N, Suzuki Y, Tsuge T, Okumura K, Ra C, and Tomino Y (2002) FcRn-mediated transcytosis of immunoglobulin G in human renal proximal tubular epithelial cells. *Am J Physiol Renal Physiol* **282:**F358–F365.

Labrijn AF, Buijsse AO, van den Bremer ET, Verwilligen AY, Bleeker WK, Thorpe SJ, Killestein J, Polman CH, Aalberse RC, Schuurman J, et al. (2009) Therapeutic IgG4 antibodies engage in Fab-arm exchange with endogenous human IgG4 in vivo. *Nat Biotechnol* **27:**767–771.

Labrijn AF, Janmaat ML, Reichert JM, and Parren PWHI (2019) Bispecific antibodies: a mechanistic review of the pipeline. *Nat Rev Drug Discov* **18:**585–608.

Lawrence MG, Altenburg MK, Sanford R, Willett JD, Bleasdale B, Ballou B, Wilder J, Li F, Miner JH, Berg UB, et al. (2017) Permeation of macromolecules into the renal glomerular basement membrane and capture by the tubules. *Proc Natl Acad Sci USA* **114:**2958–2963.

Ma J, Mo Y, Tang M, Shen J, Qi Y, Zhao W, Huang Y, Xu Y, and Qian C (2021) Bispecific antibodies: from research to clinical application. *Front Immunol* **12:**626616.

Molskness TA, Stouffer RL, Burry KA, Gorrill MJ, Lee DM, and Patton PE (2004) Circulating levels of free and total vascular endothelial growth factor (VEGF)-A, soluble VEGF receptors-1 and -2, and angiogenin during ovarian stimulation in non-human primates and women. *Hum Reprod* **19:**822–830.

Nobis M, Warren SC, Lucas MC, Murphy KJ, Herrmann D, and Timpson P (2018) Molecular mobility and activity in an intravital imaging setting - implications for cancer progression and targeting. *J Cell Sci* **131:**jcs206995.

Pyzik M, Rath T, Lencer WI, Baker K, and Blumberg RS (2015) FcRn: the architect behind the immune and nonimmune functions of IgG and albumin. *J Immunol* **194:**4595–4603.

Rock BM and Foti RS (2019) Pharmacokinetic and drug metabolism properties of novel therapeutic modalities. *Drug Metab Dispos* **47:**1097–1099.

Roopenian DC and Akilesh S (2007) FcRn: the neonatal Fc receptor comes of age. *Nat Rev Immunol* **7:**715–725.

Ryan J, Morgan RE, Chen Y, Volak LP, Dunn RT 2nd, and Dunn KW (2018) Intravital multiphoton microscopy with fluorescent bile salts in rats as an in vivo biomarker for hepatobiliary transport inhibition. *Drug Metab Dispos* **46:**704–718.

Sandoval, R. M., and B. A. Molitoris. 2013. Quantifying glomerular permeability of fluorescent macromolecules using 2-photon microscopy in Munich Wistar rats. *J Vis Exp* **74:**50054.

Sandoval RM, Wagner MC, Patel M, Campos-Bilderback SB, Rhodes GJ, Wang E, Wean SE, Clendenon SS, and Molitoris BA (2012) Multiple factors influence glomerular albumin permeability in rats. *J Am Soc Nephrol* **23:**447–457.

Sandoval RM, Wang E, and Molitoris BA (2014) Finding the bottom and using it: offsets and sensitivity in the detection of low intensity values in vivo with 2-photon microscopy. *Intravital* **2:**e23674.

Sedykh SE, Prinz VV, Buneva VN, and Nevinsky GA (2018) Bispecific antibodies: design, therapy, perspectives. *Drug Des Devel Ther* **12:**195–208.

Shields RL, Namenuk AK, Hong K, Meng YG, Rae J, Briggs J, Xie D, Lai J, Stadlen A, Li B, et al. (2001) High resolution mapping of the binding site on human IgG1 for Fc γ RI, Fc γ RII, Fc γ RIII, and FcRn and design of IgG1 variants with improved binding to the Fc γ R. *J Biol Chem* **276:**6591–6604.

Silva JP, Vetterlein O, Jose J, Peters S, and Kirby H (2015) The S228P mutation prevents in vivo and in vitro IgG4 Fab-arm exchange as demonstrated using a combination of novel quantitative immunoassays and physiological matrix preparation. *J Biol Chem* **290:**5462–5469.

Tibbitts J, Canter D, Graff R, Smith A, and Khawli LA (2016) Key factors influencing ADME properties of therapeutic proteins: A need for ADME characterization in drug discovery and development. *MAbs* **8:**229–245.

Wagner MC, Myslinski J, Pratap S, Flores B, Rhodes G, Campos-Bilderback SB, Sandoval RM, Kumar S, Patel M, Ashish, et al. (2016) Mechanism of increased clearance of glycated albumin by proximal tubule cells. *Am J Physiol Renal Physiol* **310:**F1089–F1102.

Wang M, Zhan Y, O'Neil SP, Harris S, Henson C, McEwen A, Webster R, and O'Hara DM (2018) Quantitative biodistribution of biotherapeutics at whole body, organ and cellular levels by autoradiography. *Bioanalysis* **10:**1487–1500.

Williams SP, Ogasawara A, Tinianow JN, Flores JE, Kan D, Lau J, Go M, Vanderbilt AN, Gill HS, Miao L, et al. (2016) ImmunoPET helps predicting the efficacy of antibody-drug conjugates targeting TENB2 and STEAP1. *Oncotarget* **7:**25103–25112.

Xin Y, Li J, Wu J, Kinard R, Weekes CD, Patnaik A, Lorusso P, Brachmann R, Tong RK, Yan Y, et al. (2012) Pharmacokinetic and pharmacodynamic analysis of circulating biomarkers of anti-NRP1, a novel antiangiogenesis agent, in two phase I trials in patients with advanced solid tumors. *Clin Cancer Res* **18:**6040–6048.

Address correspondence to: Amita Datta-Mannan, Eli Lilly and Company, Lilly Research Laboratories, Lilly Corporate Center, Indianapolis, IN 46225. E-mail: datta_amita@lilly.com; or Kenneth W. Dunn, Department of Medicine, Division of Nephrology, Indiana University School of Medicine, 950 W. Walnut St., Indianapolis, IN 46202.